Oral presentation | Fluid-structure interaction

Fluid-structure interaction-IV

Tue. Jul 16, 2024 10:45 AM - 11:45 AM Room A

[4-A-01] A Front-Tracking Technique for Computing Inflatable Structures in Supersonic Flows with Shocks

Valerio Orlandini[1], Alessia Assonitis[1], Renato Paciorri[1], *Aldo Bonfiglioli[2] （1. University of Rome La Sapienza - Dept. of Mechanical and Aerospace Engineering, 2. University of Basilicata, School of Engineering）

Keywords: Front-tracking method, shock-fitting method, inflatable structure in supersonic flow

Twelfth International Conference on
Computational Fluid Dynamics (ICCFD12),
Kobe, Japan, July 14-19, 2024

A Front-Tracking Technique for Computing Inflatable Structures in Supersonic Flows with Shocks

V. Orlandini*, R. Paciorri*, A. Assonitis*, F. Saltari*, and A. Bonfiglioli**
Corresponding author: valerio.orlandini@uniroma1.it
* University of Rome “La Sapienza”, Italy.
** University of Basilicata, Italy.

Abstract: In recent years, both NASA and ESA have run Technology Demonstration Missions employing Hypersonic Inflatable Aerodynamic Decelerators (HIADs), an inflatable structure covered by a flexible heat shield which is used to decelerate and protect space vehicles entering the atmosphere at hypersonic speed. This paper describes a recently developed numerical technique to simulate the Fluid-Structure interaction between the hypersonic stream and the flexible structure of the HIAD. We do so by using a front-tracking/shock-fitting technique that models both the bow shock and the thin membrane of the HIAD as double-sided surfaces of negligible thickness. Shock-motion is governed by the Rankine-Hugoniot jump relations, whereas a non-linear membrane model is used to simulate the deformation of the HIAD under the combined effect of the inflation and aerodynamic pressure. Local re-meshing is used to ensure that the surface triangulations used to geometrically describe both the material interfaces and the bow-shock are conforming with the background tetrahedral grid that fills the fluid domain. The computational examples cover three different HIADs of increasing geometrical complexity. We also show that fitting, rather than capturing, the bow shock allows to preserve the design order of the spatial discretization scheme in the entire shock-downstream region.

Keywords: Fluid-Structrure Interaction, Hypersonic flows, Shock-capturing, Shock-fitting.

1 Introduction

Typical rigid aeroshells used to protect spacecrafts during atmospheric entry are limited in size by the launch vehicle shroud. In contrast, Hypersonic Inflatable Aerodynamic Decelerators (HIADs) - an inflatable structure protected by a flexible heat shield - are packed in a stowed configuration during launch and deployed only prior to atmospheric entry to produce an aeroshell many times larger than the diameter of the launch vehicle. A large deployable heatshield creates more drag and starts the deceleration process in the upper reaches of the atmosphere, allowing not only heavier payloads, but also landing at higher altitudes [1]. Both NASA [1, 2, 3, 4, 5] and ESA [6, 7, 8] have run Technology Demonstration Missions employing HIADs. In a recent conference paper [9], we propose to use HIADs for Drag Modulation [10] during an aerocapture manouver to compensate unforeseen variations in atmospheric density that may be encountered during re-entry and eventually lead to mission failure. In [9], drag modulation is accomplished by using a variable inflation pressure to change both the shape, hence the drag coefficient, and cross-sectional area of the HIAD during the aeocapture manouver. In the present paper we describe in detail the Fluid/Structure interaction (FSI) numerical methodology that has been used in [9] to simulate the deformation induced on the thin and flexible structure of the HIAD by the combined effect of the inflation and aerodynamic pressure. In the proposed FSI technique the thin and deformable structure of the HIAD is modeled using a front-tracking technique, i.e. it is geometrically represented as a lower dimensional manifold (a surface triangulation in the 3D space) which undergoes a Lagrangean displacement under the combined effect of the inflation pressure, acting on the inner side of the HIAD, and the aerodynamic pressure exerted on the surface of the HIAD exposed to the hypersonic stream. The use of a front-tracking approach to model thin and deformable structures is not new: it has already been used in a similar setting to study the FSI between parachutes and the surrounding fluid, see e.g. [11, 12, 13, 14].

The mutual interaction between the structure and the fluid can be handled either by using volumetric meshes that match the surface tessellation of the structure at the interface [11] or, alternatively, using Immersed Boundary techniques; see e.g. [12, 13, 14] for examples pertaining to parachutes. Our approach belongs to the former class and it is similar in this respect to the Deforming-Spatial-Domain/Stabilized Space–Time (DSD/SST) formulation reviewed in [15].

The originality of the present study is that it models gas-dynamic discontinuities in the same way as it handles material interfaces, i.e. as double-sided triangulated surfaces of discontinuity that bound regions of the flow-field where a smooth solutions to the governing PDEs exists. The space-time evolution of the gas-dynamic discontinuities, as well as their upstream/downstream flow states, are computed by enforcing the Rankine-Hugoniot (R-H) jump relations, which also provide the local speed of the discontinuity. This modeling option is known as shock-fitting (S-F) [16] and it is alternative to the shock-capturing (S-C) approach that is almost universally used in fluid-dynamics simulations within a continuum framework.

S-F allows to overcome most of the troubles suffered by S-C schemes when dealing with shocked-flows, which include: a "captured" shock-width that exceeds by orders of magnitude the physical one and the presence of spurious disturbances along the "captured" shock-front which spoil the solution in the entire shock-downstream region [17, 18, 19]. Because of this, S-F techniques allow to obtain solutions characterized by a small discretization error even on rather coarse grids.

In the unstructured-grid S-F technique developed by the authors [20, 21] the computational domain is filled with a fixed, background mesh which is locally adapted in the neighbourhood of the moving discontinuities to ensure that the volumetric tetrahedral grid is always conforming with the surface triangulation used to represent the gas-dynamic discontinuities. Following the same idea, the thin membrane of the HIAD is also modelled using surfaces of zero-thickness. However, while the displacement of the gas-dynamic discontinuities is computed by enforcing the R-H relations, the displacement/deformation of the structure induced by the combined effect of the inflation and aerodynamic pressure is computed using a structural solver.

In this paper, the aforementioned technique will be used to study the FSI between an hypersonic stream and three different HIADs of increasing geometrical complexity. We will do so under the simplifying assumption of inviscid flow. Even if ignoring viscous effects precludes the possibility of computing the heat flux on the thermal protection system, it has no effect on the FSI algorithm, which is the main focus of the present paper, and only a minor effect on the computed drag coefficient.

Structural analyses of the Inflatable Re-entry Vehicle Experiment (IRVE) HIAD are reported in [1, 22, 23]. Reference [23] also accounts for the effect of the aerodynamic pressure on the static and modal analysis of the IRVE HIAD. None of the aforementioned papers, however, can describe the two-way interaction between the deformable HIAD and the hypersonic stream, which is instead possible using the FSI technique described herein.

Algorithmic details about the proposed methodology are given in § 2 and its application to three different HIADs of increasing geometrical complexity is reported in § 3. For the simplest geometry, we include a global and local grid-convergence analysis.

2 Methodology

The three-dimensional, unstructured-grid, shock-fitting technique developed over the past decade by some of the authors [20, 21] features a modular software structure which comprises different packages: unstructured volumetric and surface mesh-generators, the shock-fitting module and an unstructured shock-capturing solver. Gasdynamic discontinuities, either shock-fronts or contact-surfaces, are geometrically modeled as double-sided triangulated surfaces of negligible tickness which can freely float throughout the computational domain. This is filled with a tetrahedral grid which is locally re-meshed in the neighbourhood of the moving discontinuities to ensure that the volumetric mesh is always conforming to the surface triangulation of the fitted discontinuities. Volumetric and surface mesh generation is accomplished using the public domain software packages `tetgen` [24] and `mmgs` [25], respectively. The shock-fitting module `UnDiFi-3D` ensures that the flow variables on the upstream and downstream sides of a discontinuity obey the Rankine-Hugoniot jump relations and also supplies the local speed of the discontinuities. These behave as internal boundaries of zero thickness for an in-house developed shock-capturing code (`eulfs` [26, 27]) which is used to discretize the governing PDEs in the smooth regions of the flow-field.

One of the appealing features of the aforementioned approach consists in the possibility of using as black boxes off-the-shelf software packages, either commercial, public-domain or in-house, all driven by the `UnDiFi-3D` S-F module. This approach adds flexibility to the technique because it allows to easily replace some of the component software packages with similar ones; for instance: we have used `GRUMMP` [28] in place of `tetgen` as tetrahedral mesh generator in [21] and the S-C solver `NEO` [29, 30, 31] instead of `eulfs` in [32].

In the present paper, we extend the `UnDiFi-3D` shock-fitting software package by making it capable to deal with the deforming membrane of the HIAD, which is modeled as a double-sided surface of zero thickness: its *inner* side is exposed to the constant inflation pressure, p_{inf}, whereas the *outer* side to the spatially variable aerodynamic pressure exerted by the fluid. Assuming constant inflation pressure is consistent with the fact that in the present study we limit ourselves to steady flows. By doing so, we avoid simulating the inflation process and prescribe a spatially constant inflation pressure on the inner side of the HIAD. The displacement of the membrane due to the differential effect of the pressure forces acting on its two sides is simulated using the non-linear structural solver available in the commercial package MSC Nastran [33].

2.1 Structural model

Inflatable objects typically undergo significant deformations, making linear analysis, which assumes small deflections and strains as well as stresses below the material's yield stress, unreliable. Therefore, studying these problems requires a nonlinear approach to account for the effects of non-linearity. In nonlinear structural analysis, deflections and stresses do not vary proportionally with the loads. The structure's response is contingent upon its current state, and the equilibrium equations acknowledge that the stiffness of the structure is influenced by both displacements and external loads. As the structure deforms under loading, its stiffness changes, which in turn alters the structure's response. Consequently, nonlinear problems require incremental solution methods that break the problem into steps: calculating displacements and then updating stiffness at each step. Each step uses the outcomes from the previous step as a starting point. This process requires frequent generation and inversion of the stiffness matrix, increasing both the time and cost of the analysis. Additionally, because the response is not proportional to the loads, each load case must be resolved independently, making the principle of superposition inapplicable.

Nonlinear effects can be classified into three categories: material non-linearity, geometric non-linearity, and nonlinear boundary conditions. Material non-linearity arises from the nonlinear relationship between stresses and strains, and large strains can further influence material behavior. Geometrically nonlinear problems involve large displacements, where "large" implies displacements that invalidate the small displacement assumptions made in linear analysis. Boundary conditions and/or loads can also induce non-linearity. For instance, a follower force may be locally non-conservative, but represent a conservative loading system when integrated over the structure, such as in the case of a pressurized cylinder.

In this paper only the geometrical and load-induced non-linearities are considered whereas the materials are linear elastic. Under these hypothesis, the equilibrium equations translate the fact that the internal stresses balance the external forces at steady-state:

$$\nabla \cdot \mathbf{P} + \mathbf{b}_0 = \mathbf{0} \tag{1}$$

In Eq. (1) $\mathbf{P}$ is the second Piola-Kirchhoff stress tensor and $\mathbf{b}_0$ is the body force per unit volume in the reference configuration.
The constitutive equations describe the material behavior and relate the stress tensor $\mathbf{P}$ to the strain tensor $\mathbf{E}$:

$$\mathbf{P} = \mathbf{C} : \mathbf{E} \tag{2}$$

The symbol ':' in Eq. (2) denotes a double contraction between the fourth-order elastic tensor $\mathbf{C}$ and the Green-Lagrange strain tensor $\mathbf{E}$:

$$\mathbf{E} = \frac{1}{2}(\mathbf{F}^T\mathbf{F} - \mathbf{I}) \tag{3}$$

where $\mathbf{F}$ is the deformation gradient tensor.

2.1.1 Updated Lagrangian Approach

Generally, deformations of structures are analyzed through a Lagrangian approach that can be classified in two alternative categories: the total Lagrangian method and the updated Lagrangian method. In the total Lagrangian approach, the equilibrium is expressed with the original undeformed state as the reference; in the updated Lagrangian approach, the current configuration acts as the reference state. In the updated Lagrangian approach used in this paper, the configuration of the structure is updated at each increment; in particular, the Green-Lagrange strain tensor $\mathbf{E}$ defined by Eq. (3) is updated through the deformation gradient given by:

$$\mathbf{F} = \frac{\partial \mathbf{x}}{\partial \mathbf{X}} \tag{4}$$

where $\mathbf{x}$ are the current coordinates and $\mathbf{X}$ are the reference coordinates. This approach is particularly useful for problems involving large deformations.

2.1.2 Finite Element formulation

The system governing equilibrium equations can be obtained by invoking the principle of virtual work [34]: for a system in equilibrium, the total virtual work, δW, done by the internal and external forces during any virtual displacement is zero:

$$\delta W = \delta W_{\text{int}} + \delta W_{\text{ext}} = 0 \tag{5}$$

In Eq. (5) δW_{int} is the work done by the internal forces (stresses) within the material when it undergoes the virtual displacement. For a continuum, this can be written as:

$$\delta W_{\text{int}} = \int_{\Omega_0} \mathbf{P} : \delta \mathbf{E}\, d\Omega_0 \tag{6}$$

δW_{ext} in Eq. (5) is the work done by the external forces (such as applied loads and reactions) during the virtual displacement and can be expressed as:

$$\delta W_{\text{ext}} = -\left(\int_{\Omega_0} \mathbf{b}_0 \cdot \delta \mathbf{u}\, d\Omega_0 + \int_{\Gamma_t} \mathbf{t}_0 \cdot \delta \mathbf{u}\, d\Gamma_0 \right) \tag{7}$$

Considering a three-dimensional continuum and a nonlinear problem, the stationary condition (5) results in:

$$\int_{\Omega_0} \mathbf{P} : \delta \mathbf{E}\, d\Omega_0 = \int_{\Omega_0} \mathbf{b}_0 \cdot \delta \mathbf{u}\, d\Omega_0 + \int_{\Gamma_t} \mathbf{t}_0 \cdot \delta \mathbf{u}\, d\Gamma_0 \tag{8}$$

where $\delta \mathbf{u}$ represents the virtual displacement, Ω_0 is the domain in the reference configuration, Γ_t is the boundary with applied tractions $\mathbf{t}_0$ and $\delta \mathbf{E}$ is the virtual strain tensor.

To discretize the domain, we divide it into finite elements. Within each element, the displacement field $\mathbf{u}$ and its variations $\delta \mathbf{u}$ are approximated using shape functions N_i:

$$\mathbf{u} \approx \sum_{i=1}^{n} N_i \mathbf{d}_i, \quad \delta \mathbf{u} \approx \sum_{i=1}^{n} N_i \delta \mathbf{d}_i$$

where $\mathbf{d}_i$ are the nodal displacements, which include linear and angular displacements and n is the number of nodes in the finite element. For surfaces discretized with quadrangular elements the Lagrangian shape functions in natural coordinates (ζ, η) are:

$$\begin{aligned}
N_1(\zeta, \eta) &= \frac{1}{4}(1 - \zeta)(1 - \eta) \\
N_2(\zeta, \eta) &= \frac{1}{4}(1 + \zeta)(1 - \eta) \\
N_3(\zeta, \eta) &= \frac{1}{4}(1 + \zeta)(1 + \eta) \\
N_4(\zeta, \eta) &= \frac{1}{4}(1 - \zeta)(1 + \eta)
\end{aligned}$$

In the FEM formulation, strains and nodal displacements are related by the strain-displacement matrix $\mathbf{B}$ which involves derivatives of the shape functions with respect to reference coordinates. For a surface element, $\mathbf{B}$ is constructed as:

$$\mathbf{B} = \begin{bmatrix} \frac{\partial N_1}{\partial X} & 0 & \frac{\partial N_2}{\partial X} & 0 & \cdots & \frac{\partial N_n}{\partial X} & 0 \\ 0 & \frac{\partial N_1}{\partial Y} & 0 & \frac{\partial N_2}{\partial Y} & \cdots & 0 & \frac{\partial N_n}{\partial Y} \\ \frac{\partial N_1}{\partial Y} & \frac{\partial N_1}{\partial X} & \frac{\partial N_2}{\partial Y} & \frac{\partial N_2}{\partial X} & \cdots & \frac{\partial N_n}{\partial Y} & \frac{\partial N_n}{\partial X} \end{bmatrix} \tag{9}$$

The Green-Lagrange strain tensor $\mathbf{E}$ in Eq. (3) can then be written as follows:

$$\mathbf{E} = \frac{1}{2}[\mathbf{Bd} + (\mathbf{Bd})^T + (\mathbf{Bd})^T(\mathbf{Bd})] \tag{10}$$

and the discretized form of the equilibrium equations (8) for an element becomes:

$$\mathbf{K}\mathbf{d} = \mathbf{f} \tag{11}$$

where $\mathbf{K}$ is the element stiffness matrix, $\mathbf{d}$ is the vector of nodal displacements, and $\mathbf{f}$ is the vector of nodal forces. The element stiffness matrix $\mathbf{K}$ is given by:

$$\mathbf{K} = \int_{V_e} \mathbf{B}^T \mathbf{C} \mathbf{B} \, dV \tag{12}$$

where V_e is the volume of the element and $\mathbf{C}$ is the energy tensor, see Eq. (2).

The nodal force vector $\mathbf{f}$ includes contributions from external forces and body forces:

$$\mathbf{f} = \int_{V_e} \mathbf{N}^T \mathbf{b} \, dV + \int_{S_e} \mathbf{N}^T \mathbf{t} \, dS \tag{13}$$

where $\mathbf{b}$ is the body force per unit volume and $\mathbf{t}$ is the traction force per unit area on the surface S_e.

2.1.3 Iterative solution strategy

The Newton-Raphson method is here used to iteratively solve the system of algebraic equations arising from the FEM discretization of the equilibrium condition. The system of equations is nonlinear, because element nodal forces are nonlinear functions of displacements. Since the error vanishes at constrained points and the constraint forces vanish at free points, the unbalanced forces acting at nodal points at any iteration step are conveniently defined as an iterative convergence monitor by defining the residual vector $\mathbf{R}$:

$$\mathbf{R}^i = \mathbf{f}_{\text{ext}} - \mathbf{f}_{\text{int}} \left(\mathbf{d}^i \right) \tag{14}$$

where $\mathbf{f}_{\text{ext}}$ is the external force vector, $\mathbf{f}_{\text{int}}$ is the internal force vector and the superscript i indicates the iteration counter.

The displacement vector is updated iteratively as:

$$\mathbf{d}^{i+1} = \mathbf{d}^i + \Delta \mathbf{d} \tag{15}$$

where $\Delta\mathbf{d}$ is the solution to the linear system:

$$\mathbf{K}_T^i \Delta \mathbf{d} = \mathbf{R}^i \tag{16}$$

The tangential stiffness matrix $\mathbf{K}_T$:

$$\mathbf{K}_T = \frac{\partial \mathbf{R}}{\partial \mathbf{d}} \tag{17}$$

that appears in Eq. (16) is the sum of the material stiffness, $\mathbf{K}^m$, and differential stiffness, $\mathbf{K}^d$:

$$\mathbf{K}_T = \mathbf{K}^m + \mathbf{K}^d \tag{18}$$

The differential stiffness, which is caused by the initial stress, can be written as follows:

$$\mathbf{K}^d = \int_{V_e} \mathbf{G}^T \mathbf{M} \mathbf{G} \, dV, \tag{19}$$

where matrix $\mathbf{G}$ consists of derivatives of the shape functions and matrix $\mathbf{M}$ is a function of the stresses.

The iterative scheme consists in repeatedly solving the linear system (16) and updating the displacement vector according to (15) until the residual error $\mathbf{R}$ and the incremental displacements $\boldsymbol{\Delta}\mathbf{d}$ become negligibly small.

2.1.4 Verification case

As a verification test, we study the case of a side wind impacting an hemispherical dome. In this scenario, the governing equations for shells of revolution under a non-axisymmetric load can be written as follows using spherical coordinates:

$$\begin{gathered}\frac{\partial}{\partial \varphi}(r_0 N_{\theta\varphi}) + \frac{\partial N_\theta}{\partial \theta} r_1 + N_{\theta\varphi} r_1 \cos\varphi + p_\theta r_0 r_1 = 0 \\ \frac{\partial}{\partial \varphi}(r_0 N_{\varphi}) + \frac{\partial N_{\theta\varphi}}{\partial \theta} r_1 - N_{\theta} r_1 \cos\varphi + p_\varphi r_0 r_1 = 0 \\ \frac{N_\varphi}{r_1} + \frac{N_\theta}{r_2} = -p_z \end{gathered} \tag{20}$$

In Eq. (20) r_0, r_1, r_2 are curvature radii: the first two related to the parallel (θ) and the meridian direction (φ), respectively, whereas r_2 is the distance between the generic surface material point and the intersection between the curvature radius and the rotational axis, see Fig.1. For the purpose of the present analysis, which is applied to a spherical shell of radius $a = 1$ m, we have:

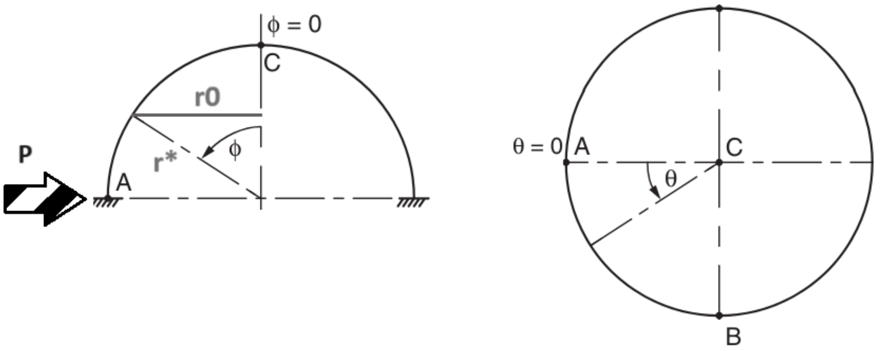

Figure 1: Hemispherical dome subjected to wind loading

$$r_1 = r_2 = r^* = 1 \text{ m}$$

and

$$r_0 = r^* \sin\varphi.$$

In Eq. (20) $p_\vartheta, p_\varphi, p_z$ are the components of the external load whereas N_θ and N_φ are the two membrane forces per unit length and $N_{\theta\varphi}$ is the shear force.

If we neglect frictional forces and assume that the force exerted by the wind has only one non-zero component along the z axis:

$$p_\vartheta = 0 \qquad p_\varphi = 0 \qquad p_z = p_\infty \sin\varphi \cos\vartheta \tag{21}$$

where $p_\infty = 100$ bar, the system of PDEs (20) simplifies and admits the following analytical solution due to Zingoni [35]:

$$\begin{aligned} N_{\theta\varphi} &= \frac{p_\infty a}{3}\left(\frac{\cos\varphi}{\sin^3\varphi}\right)\left[(3-\cos^2\varphi)\cos\varphi - 2\right]\cos\theta \\ N_\varphi &= \frac{p_\infty a}{3}\left(\frac{1}{\sin^3\varphi}\right)\left[(3-\cos^2\varphi)\cos\varphi - 2\right]\sin\theta \\ N_\theta &= -\frac{p_\infty a}{3}\left(\frac{1}{\sin^3\varphi}\right)\left(\left[(3-\cos^2\varphi)\cos\varphi - 2\right]\cos\varphi + 3\sin^4\varphi\right)\cos\theta \end{aligned} \tag{22}$$

which we use here to validate the numerical methodology. For the FEM solution we have considered an hemispherical dome, 1 mm thick, made of Kevlar, which is characterized by a value of Young's modulus $E = 70$ GPa and Poisson's ratio $\nu = 0.35$. Figure 2 compares the analytical and numerical solutions in the final configuration. Figure 2a shows the displacement and Fig. 2b the three dimensionless forces, as a function of the angle φ. $N_{\theta\varphi}$ has been plot for an angle θ equal to 90° whereas the other two forces at $\theta = 0°$. The agreement between the analytical and numerical solutions is very good.

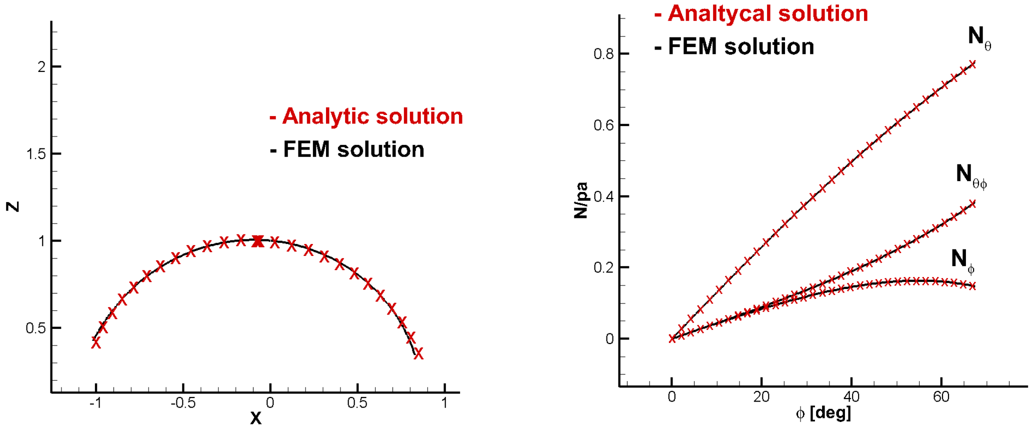

(a) Displacements

(b) Membrane forces

Figure 2: Comparison between the analytical and FEM solutions.

2.2 Fluid model

As far as the fluid model is concerned, we consider the numerical approximation of solutions of the steady limit of the Euler equations reading:

$$\partial_t \mathbf{U} + \nabla \cdot \mathbf{F} = 0 \quad \text{in} \quad \Omega \subset \mathbb{R}^d \tag{23}$$

with conserved variables and fluxes given by:

$$\mathbf{U} = \begin{bmatrix} \rho \\ \rho E \\ \rho \mathbf{u} \end{bmatrix} , \quad \mathbf{F} = \begin{bmatrix} \rho \mathbf{u} \\ \rho H \mathbf{u} \\ \rho \mathbf{u}\mathbf{u} + p\mathbb{I} \end{bmatrix} \tag{24}$$

having denoted by ρ the mass density, by $\mathbf{u}$ the velocity, by p the pressure, and with $E = e + \mathbf{u} \cdot \mathbf{u}/2$ the specific total energy, e being the specific internal energy. Finally, the total specific enthalpy is $H = h + \mathbf{u} \cdot \mathbf{u}/2$, with $h = e + p/\rho$ the specific enthalpy. For simplicity in this paper we work with the classical perfect gas equation of state:

$$p = (\gamma - 1)\rho e \tag{25}$$

γ being the adiabatic index.

In all applications involving high-speed flows, solutions of (23) are only piecewise continuous. In d space dimensions, discontinuities are represented by $d - 1$ manifolds governed by the well known Rankine-Hugoniot jump conditions reading:

$$[\![\mathbf{F} \cdot \mathbf{n}]\!] = w[\![\mathbf{U}]\!] \tag{26}$$

having denoted by $\mathbf{n}$ the local normal vector to the shock, by $[\![\cdot]\!]$ the corresponding jump of a quantity across the discontinuity, and with w the normal component of the shock speed.

Even if ignoring viscous effects precludes the possibility of computing the heat flux on the thermal shield, it has no effect on the FSI algorithm, which is the main focus of the present paper, and is expected to play only a minor role on the computed drag coefficient.

2.2.1 CFD model

Concerning the `eulfs` in-house solver used in this paper, it is based on a *Residual Distribution (RD)* method evolving in pseudo-time approximations of the values of the flow variables in the mesh nodes. To be more specific, Roe's parameter vector, $Z = \sqrt{\rho}\,(1, H, \mathbf{u})^t$, is chosen as the set of dependent variables which vary linearly and continuously in space among the vertices of a tetrahedral mesh that fills the computational domain. The method has several appealing characteristics, including the possibility of defining genuine multidimensional upwind strategies for Eulerian flows. By combining ideas from both

Table 1: Supersonic compressible source flow: characteristics of the three grid levels used

grid level	grid-points	tetrahedra	mesh spacing h
1	10,386	48,880	$1.199\ 10^{-1}$
2	68,485	366,442	$6.130\ 10^{-2}$
3	496,161	2,868,290	$3.087\ 10^{-2}$

the stabilized finite element and finite volume methods, RD schemes allow to achieve second order of accuracy and monotonicity preservation with a compact stencil of distance-1 neighbors. Second order of accuracy in smooth flows will be demonstrated in § 2.2.2. The interested reader can refer to [36, 37] and references therein for an in-depth review of this family of methods, as well as to [26, 27] for some specific choices of the implementation used in the `eulfs` code.

When RD schemes are used to discretize the conservation-law-form (23) of the governing PDEs, the method is shock-capturing. It is however also possible to explicitly keep track of the motion of the discontinuities in the flow-fields and use the `eulfs` solver to discretize the governing PDEs in the smooth region of the flowfield bounded by the fitted discontinuities. This latter approach is what we refer to as "shock-fitting". One remarkable advantage of S-F over S-C is the capability of the former to preserve the design order of the spatial discretization scheme also downstream of a shock. In contrast, the order-of-accuracy of a S-C discretization degrades to first in the entire shock-downstream region. This is discussed in [19] for the 2D case and will be addressed in § 3.1 for the 3D case.

2.2.2 Verification case

In this section we verify that the spatial discretization scheme available in the `eulfs` CFD code recovers the design (second) order-of-accuracy in regions of smooth (shockless) flow. We do so by using an analytical solution of the Euler equations describing a compressible, supersonic source flow in 3D. Indeed, by assuming that the only non-zero component of the fluid velocity is in the radial direction, it is easy to show that the Euler equations, written using spherical coordinates, become identical to the Q1D Euler equations describing variable-area flows, provided that the area varies quadratically with the distance from the origin of the reference frame. This allows us to use the so-called area rule:

$$f\left(M\right)=\frac{1}{M}\left[\frac{2}{\gamma+1}\left(1+\frac{\gamma-1}{2}M^2\right)\right]^{\frac{\gamma+1}{2(\gamma-1)}}=\left(\frac{r}{r_*}\right)^2$$

to compute the radial distribution of the Mach number.

The computational domain consists in a spherical annulus of inner and outer radii respectively equal to $r_i=1$, $r_o=1.5$. It has been discretized using three tetrahedral meshes of decreasing mesh spacing, h, whose characteristics are given in Tab. 1.

The flow is fully supersonic with $M\left(r_i\right)=2$ all along the inner radius which implies that $r_*=r_i/\sqrt{f(2)}=0.7698$ and $M\left(r_o\right)=2.8854$.

Given a pair of solutions available on two grid-levels of mesh spacing h and rh, both a *local* (i.e. pointwise) and a *global* measure (in the L_p-norm) of the observed order-of-accuracy can be respectively calculated as follows:

$$\tilde{n} = \frac{\log\left(1/R\right)}{\log\left(r\right)} \tag{27a}$$

$$\tilde{n} = \frac{\log\left(L_p\left(\epsilon_{rh}\right)/L_p\left(\epsilon_h\right)\right)}{\log\left(r\right)} \tag{27b}$$

where the grid convergence ratio [38, 39, 40, 41] is defined as:

$$R=\epsilon_h\left(\mathbf{x}\right)/\epsilon_{rh}\left(\mathbf{x}\right) \tag{28}$$

and can only be computed within the grid-points of the coarser grid level rh, provided that the grids are nested.

In Eqs. (27b) and (28) ϵ_h is the discretization error, i.e. the difference between the value computed on grid level h and the analytical value; $\mathbf{x}$ in Eq. (28) is the location of a grid-point shared by the two nested grid levels.

Table 2 shows the L_2-norm of the discretization error measured globally using Eq. (27b) for each component of the parameter vector and all three grid levels. It can be seen that the measured order $\tilde{n}$ does indeed recover design order.

Table 2: Supersonic compressible source flow: L_2-norm of the discretization error and global order estimate

	$\sqrt{\rho}$		$\sqrt{\rho}H$		$\sqrt{\rho}u$		$\sqrt{\rho}v$		$\sqrt{\rho}w$	
level	L_2	$\tilde{n}$	L_2	$\tilde{n}$	L_2	$\tilde{n}$	L_2	$\tilde{n}$	L_2	$\tilde{n}$
1	0.2907E-02	-	0.3034E-02	-	0.1629E-02	-	0.1618E-02	-	0.1617E-02	-
2	0.8068E-03	1.91	0.8064E-03	1.98	0.4232E-03	2.01	0.4245E-03	1.99	0.4226E-03	2.00
3	0.2111E-03	1.95	0.2075E-03	1.98	0.1091E-03	1.98	0.1092E-03	1.98	0.1090E-03	1.98

2.3 Loosely coupled S-F/FSI algorithm

In the proposed FSI algorithm, the structural and CFD models resp. described in § 2.1 and § 2.2 are loosely coupled in the sense that CFD simulations are performed while keeping the structure still and structural simulation use a spatially-variable, but time-independent loading due to the differential effect of the aerodynamic and inflation pressure acting on the outer, resp. inner side of the HIAD. Only a few iterations are required until the shape of the HIAD settles to a steady configuration and so does the aerodynamic loading exerted on its outer side by the incoming hypersonic stream. The loose coupling between the structural and fluid models is justified by the fact that we are only interested in the steady configuration corresponding to a given inflation pressure.

To illustrate the algorithmic ingredient of the proposed S-F/FSI technique, we consider the hypersonic flow past an HIAD; this is characterized by the formation of a standing bow shock and the deformation of the membrane under the action of the aerodynamic and inflation pressures. To initialize the S-F/FSI simulation, we run a shock-capturing calculation (using the `eulfs` code) of the flow past the HIAD, treated as a rigid body. We do so not only to obtain an initial solution, but also an initial shock-shape; details concerning the creation of the initial shock-surface can be found in [21]. We then create a tetrahedral mesh that surrounds both the bow shock and the HIAD; it will hereafter be referred to as the "background" mesh and for the current example it fills the hemispherical volume shown in the left frame of Fig. 3. The bow-shock and the inflatable wall are geometrically modelled using surfaces of zero thickness; those shown in Fig. 3, resp. coloured in blue and green, are the initial shock-shape and the shape of the HIAD when filled at the design inflation pressure.

The S-F/FSI algorithm can be split into the following four main steps:

1. *Step 1: generation of the computational mesh*
   The first step consists in inserting the surface meshes of both the bow shock and the HIAD inside the background tetrahedral grid, as shown in Fig. 3. To do so, all tetrahedral cells of the background mesh that are crossed by either the bow-shock or the HIAD are removed and cavities are carved around those surfaces inside the background mesh. The `tetgen` mesh-generator is then used to fill these cavities using a Delaunay tetrahedralization which is constrained to be conformal with the surface triangulations of both the bow-shock and the HIAD. Moreover, all tetrahedral cells that fill the volume facing the inner side of the HIAD are also removed. This is because, as mentioned earlier, as long as we are simulating steady flows, we can prescribe a spatially uniform inflation pressure on the inner side of the HIAD and avoid simulating the inflation process. Cell removal and local re-meshing as described above leads to what we call the "computational" mesh which differs from the "background" mesh only in the neighbourhood of the bow-shock and the surface of the HIAD and because the "computational" mesh has no tetrahedra attached to the inner side of the HIAD.

2. *Step 2: Computation of the flow solution using the* CFD solver
   The `UnDiFi-3D` S-F algorithm is used to compute the CFD solution while the shape of the HIAD is held fixed. This is an iterative process even when dealing with steady flows, because the "computational" mesh changes between subsequent iterations due to the Lagrangean motion of the shock surface, which is computed by enforcing the Rankine-Hugoniot jump relations between the upstream and downstream sides of the discontinuity. The `eulfs` code is used to solve the governing PDEs in the (smooth) regions of the flow-field bounded by the surfaces of discontinuity. When

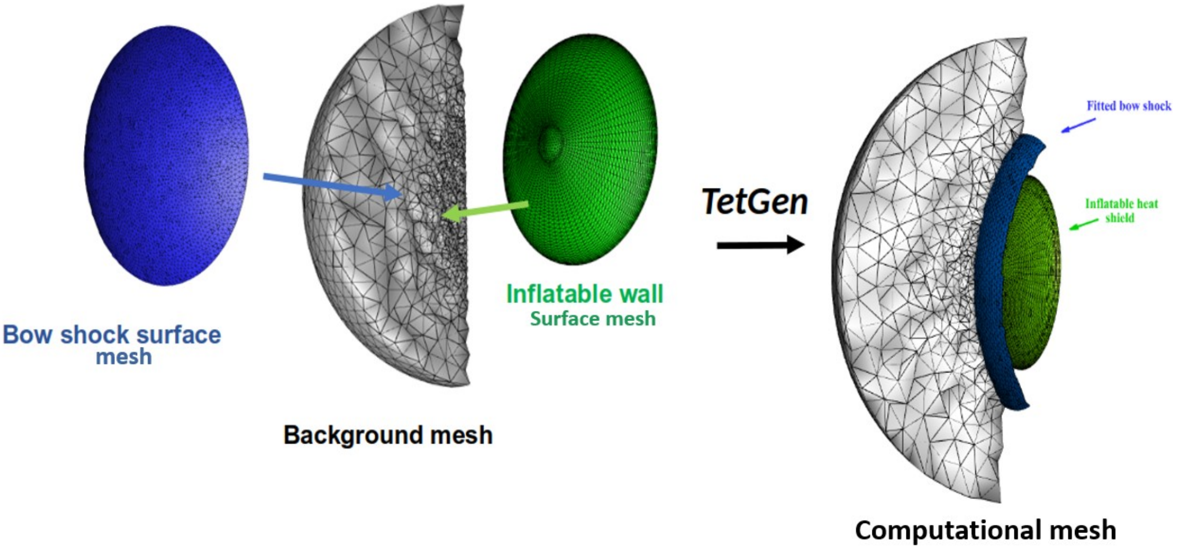

Figure 3: Step 1 of S-F/FSI algoritm: generation of the computational mesh

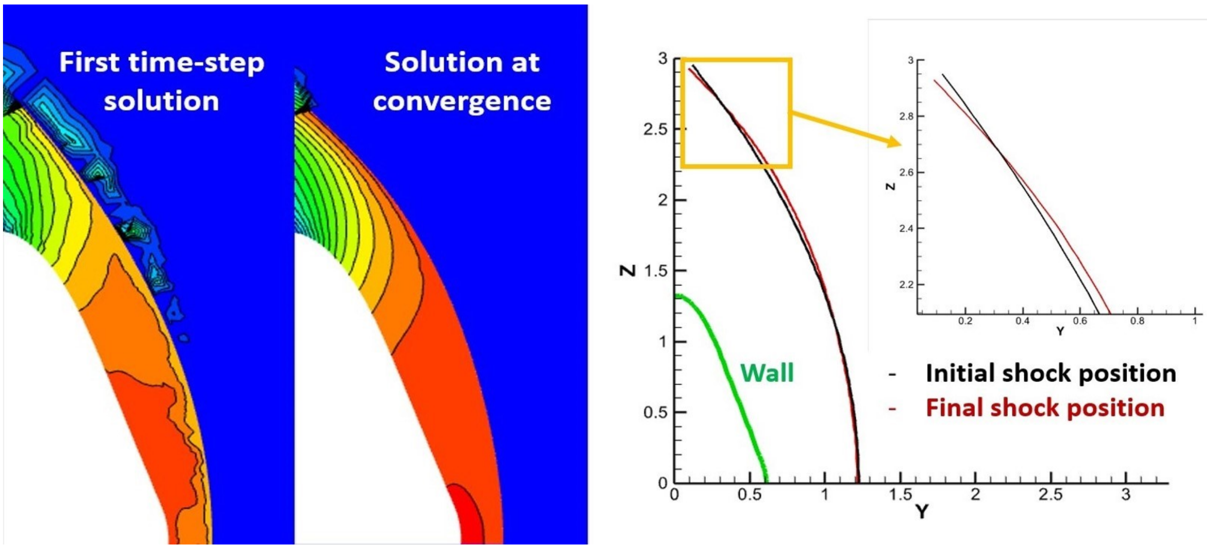

Figure 4: Step 2 of FSI algoritm: CFD solution

a steady solution exists, the shock speed asymptotically vanishes, the fitted shock surface(s) no longer move and the "computational" mesh no longer changes. The iterative process is illustrated in Fig. 4: the left frame shows the initial and the steady-state flow-fields whereas the right frame shows the initial and steady shape of the bow shock. Observe that the shape of the HIAD remains unchanged. The interested reader can find full details of the algorithm in [20, 21].

3. *Step 3: Computation of the deformation of the HIAD by means of the structural solver.* As already mentioned in § 2.1.2, the structural displacement/deformation of the HIAD is computed using the MSC Nastran [33] commercial software package that uses the structural model described in § 2.1. As skematically shown in Fig. 5, the input data are the constant inflation pressure, p_{inf}, acting on the inner side of the HIAD, shown using red vectors, and the spatially variable aerodynamic pressure load computed by the `eulfs` code on the outer side, shown using black vectors. Since we only deal with steady problems, the inertial effects of the HIAD are ignored in the structural simulation and, therefore, its displacement/deformation, shown in Fig. 6, only depends on the differential pressure acting on its two sides and on the elasticity of the membrane. This simplifies the structural model and allows to compute the inflation and deflation behavior of the HIAD as a sequence of quasi-stationary solutions.

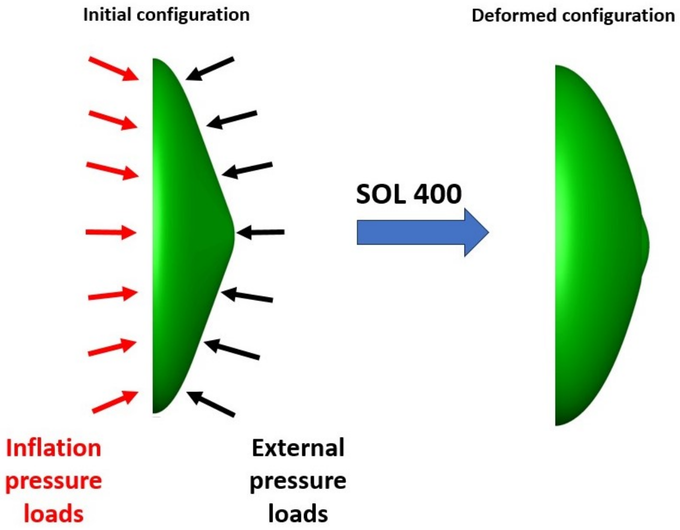

Figure 5: Step 3 of S-F/FSI algoritm: SOL 400 is used to compute the structural displacements

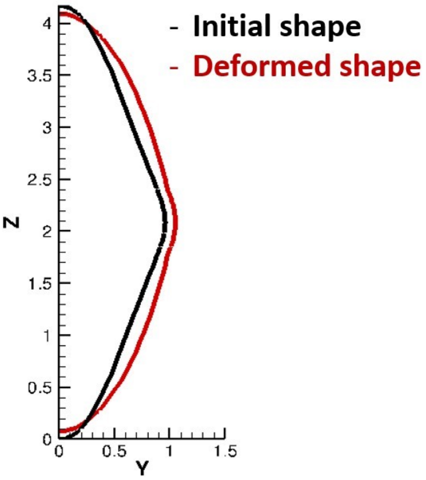

Figure 6: Deformation of the membrane due to the differential effect of the external and inflation pressure loads

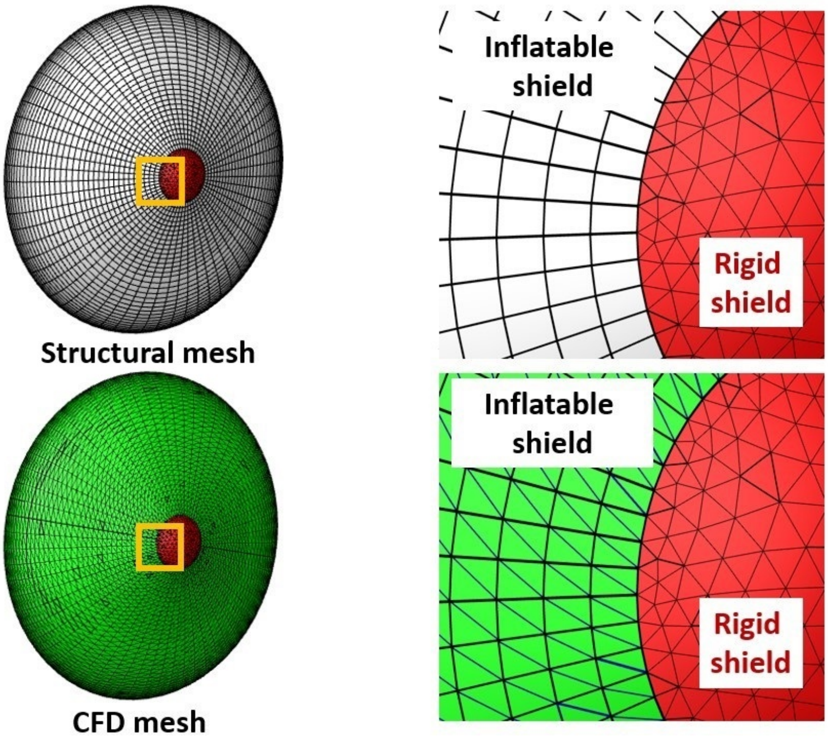

Figure 7: Coupling between the structural and CFD meshes

One algorithmic aspect which is worth underlying, see Fig.7, is that the mesh of the HIAD, except for the rigid nose, is made of quadrilateral elements, see § 2.1.2, whereas the `eulfs` CFD solver works with tetrahedral volume elements and surface triangulations. We have chosen CQUAD4 quadrilateral elements for the structural discretization because, according to the MSC software user-guide [42], they are less stiff and more accurate than their triangular counterpart, particularly for membrane strain. Therefore, when a new (deformed) shield shape is inserted into the background mesh, as we do in Step 4, the quadrilateral surface mesh of the HIAD must be converted into a triangular one. As shown in Fig. 7, this is easily accomplished by splitting each quadrilateral cell into two triangles while preserving the same geometrical location of the grid-points defining the shield in the two (quadrilateral and triangular) surface meshes. This is important to avoid interpolation when the pressure force computed by the CFD code has to be transferred to the structural solver.

4. *Step 4: Displacement of the deformable shield and interpolation*
   The updated shape of the inflatable shield is computed using the nodal displacement supplied by the structural solver in Step 3. Due to the motion of the inflatable shield, some of the grid-points of the background mesh that had been removed in Step 1 might be reintroduced at a subsequent S-F/FSI iteration. This is explained by reference to Fig. 8. Fig. 8(a) shows the initial shape of the HIAD (drawn in green) laid on top of the background tetrahedralization: the grid-points marked in red are removed in Step 1, because they fall inside the volume occupied by the initial shield shape. At a subsequent S-F/FSI iteration the shield has moved to a new location in space and has a different shape: this is shown in green in Fig. 8(b), where the initial shield shape is also drawn in grey. Some of the grid-points of the background mesh that had been removed during the first iteration (marked in red in Fig. 8(c)) remain "silent", because they fall inside the updated location of the HIAD. However, the grid-points marked in blue in Fig. 8(c) will be part of the "computational" mesh at the next S-F/FSI iteration. Therefore, it is necessary to ensure that all grid-points of the background mesh store valid flow variables at all S-F/FSI iterations. This is accomplished using interpolation from the current "computational" mesh (which keeps changing between subsequent S-F/FSI iterations unless steady-state has been reached) and the fixed "background" mesh. Note, however, that interpolation is limited to those grid-points of the background mesh that had been removed in Step 1, which is small fraction of the total number of grid-points of the background mesh.

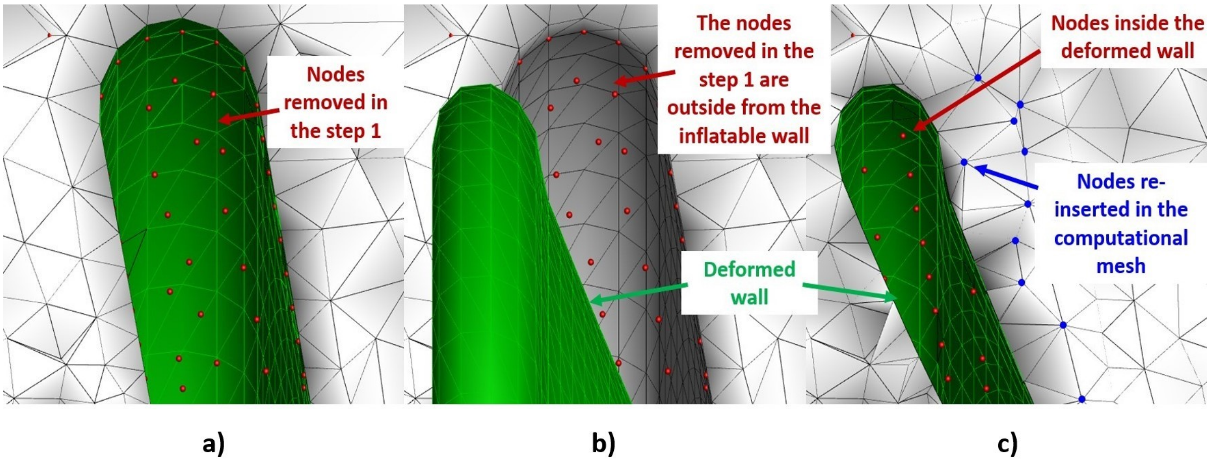

Figure 8: a) Nodes removed in Step-1 at iteration n; b) Grid-points of the background mesh that fall outside the shield in Step-4 of iteration n; c) Grid-points (marked in red) of the "background" mesh that fall inside the updated shield shape and those (marked in blue) which will be part of the "computational" mesh at Step-1 of iteration $n+1$

3 Hypersonic FSI simulations

Three different FSI test-cases involving inviscid high-speed flows will be presented and discussed: for each configuration, we provide details on both the structural modelling and CFD solution, highlighting the advantages offered by the S-F technique. Furthermore, computed results for the first test-case, see § 3.1, will be analyzed to evaluate the grid convergence properties of the technique.

3.1 Test-case 1: inflatable shield

The first test-case consists in the hypersonic, $M_\infty = 24$, flow past an HIAD whose design shape has the same geometry of the shield used in the Mars Pathfinder mission [43]. This is shown in Fig. 9(c), where its geometrical features are indicated.

Flight conditions, listed in Tab. 3, are compatible with an aerocapture mission on Mars, which is one of the viable applications for HIADs, see [9]. In Tab. 3 ρ_∞ and p_∞ respectively denote the atmospheric density and pressure at 50 km of altitude, γ is the specific heat ratio and R the specific gas constant of carbon dioxide, the primary component of the Martian atmosphere, p_{st} is the static pressure measured in the stagnation point, i.e. the stagnation pressure, and T^0_∞ is total temperature, which is constant throughout the flow-field for an inviscid, steady flow. Figures 9(a) and 9(b) respectively show the three-dimensional domain (an hemisphere of radius equal to 3.2 m) and the prescribed boundary conditions. Figure 9(c) shows the design shape of the shield which is characterized by a rigid nose, marked in red and by an inflatable part, marked in green. The initial bow shock position is extracted from the S-C solution shown in Fig. 10(c). A parabola passing through the three points circled in Fig. 10(b) is generated first and then revolved around the Y-axis to create the initial shock-surface shown in Fig. 10(c).

Mach	ρ_∞	p_∞	γ	R	p_{st}	T^0_∞
24	$9.74 \cdot 10^{-5}$ kg/m^3	3.23 Pa	1.33	191 J/kgK	2307 Pa	16710.96 K

Table 3: Atmospheric conditions encountered during an aerocapture mission on Mars

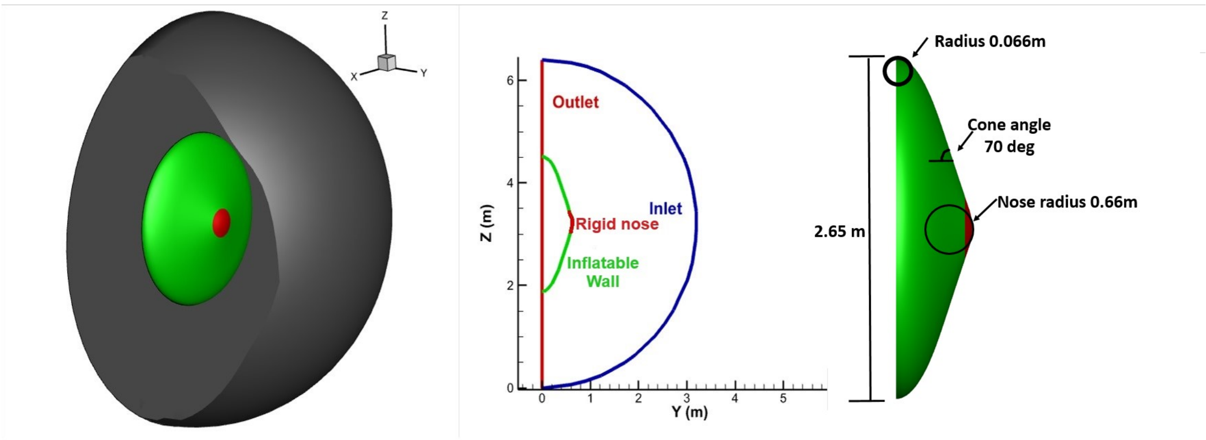

a) b) c)

Figure 9: a) 3D domain; b) Boundary conditions of the domain in YZ plane; c) Initial geometry of the shield

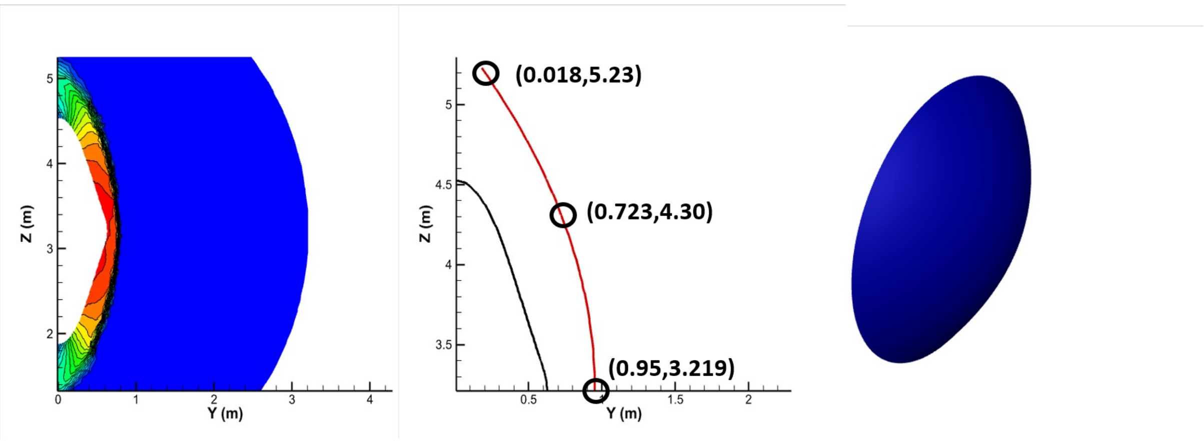

a) b) c)

Figure 10: a) S-C solution in YZ plane; b) undeformed shield and parabola approximating the bow shock in the YZ plane; c) initial shock-surface.

3.1.1 Computational grids

For this test-case, two nested background tetrahedral grids have been generated in order to also evaluate the grid-convergence properties of the discretization. The finest background grid is obtained by splitting each cell of the coarsest one into eight tetrahedra; the coarse-grid surface triangulations of both the inflatable shield and the bow-shock are similarly split into four nested triangular elements, as shown in Fig. 11. Table 4 reports the number of grid-points and cells of the volume and surface meshes for both grid-levels.

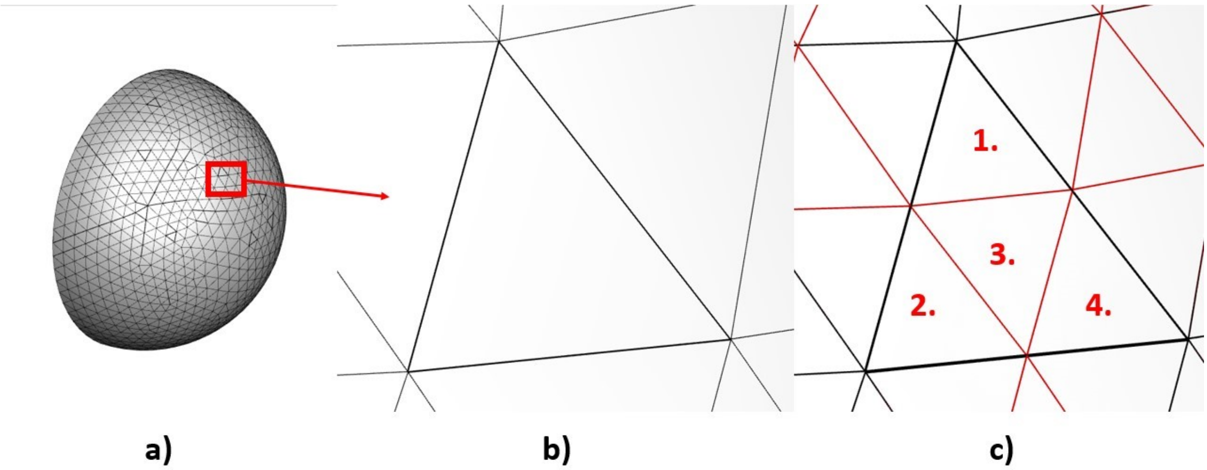

Figure 11: a) and b) coarse surface triangulations; c) each triangular element of the coarser mesh is split into four nested triangles.

Grid	Background		HIAD		Shock	
level	grid-points	tetrahedra	grid-points	triangles	grid-points	triangles
1	11020	60285	2400	4770	2053	4032
2	88158	482280	9600	19080	8212	16128

Table 4: Number of grid-points for both grid-levels

3.1.2 Structural model

The structural model is specific to the configuration under analysis and is crucial for understanding how the structure deforms. In the present test-case, both the rigid nose and the deformable surface of the HIAD are 1 mm thick and made of Kapton [44], which is assumed to be an isotropic elastic material with Young's Modulus $E = 2.6$ GPa, Poisson's ratio $\nu = 0.34$ and density $\rho_m = 1420$ kg/m^3. The following constraints have been prescribed to simulate the behavior of the inflatable shield:

- the grid-points that belong to the nose of the shield, marked in red in Fig. 12, are constrained to move only in the flow direction by the same quantity, i.e. the Y-axis of Fig. 12; by doing so, the nose behaves as a rigid part.
- The grid-points located on the outer crown (the shoulder) of the inflatable structure, marked in blue in Fig. 12, can only move in the XZ-plane, i.e. the flow-normal direction;
- the rotational degrees of freedom of the structural model have been constrained in order to enhance the convergence of the structural simulations and to overcome buckling problems, as suggested in [45, 46].

The constraints applied to the rigid nose and the outer crown allow to simulate the typical inflation and deflation characteristics of these structures.

The results to be presented in the following paragraph have been obtained using an inflation pressure $p_{\text{inf}} = 3462$ Pa, which corresponds to 1.5 times the stagnation pressure reported in Tab. 3.

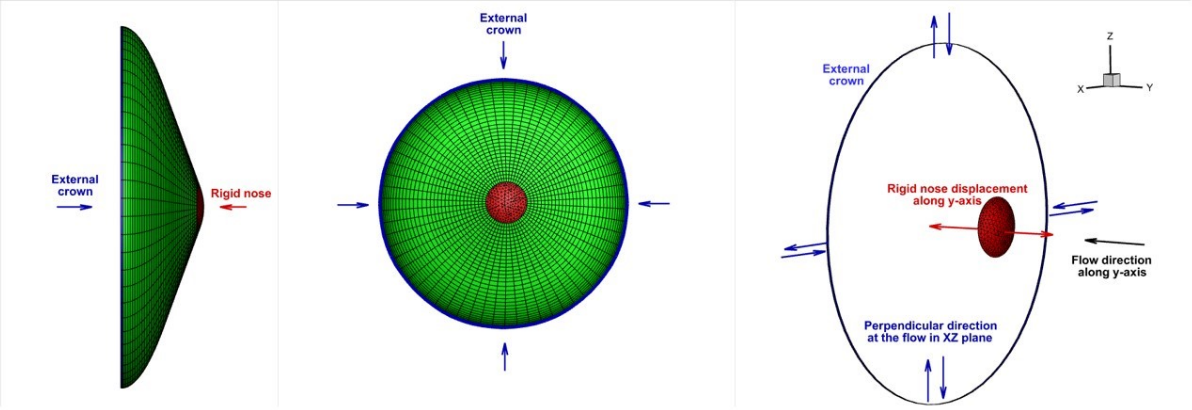

Figure 12: Structural model of the inflatable shield

3.1.3 Results

The purpose of the simple test-case is twofold: illustrating the iterative convergence properties of the S-F/FSI algorithm and demonstrating that fitting (rather than capturing) shock-waves allows to preserve the design order of the scheme in the entire shock-downstream region.

As far as iterative convergence is concerned, Fig. 13 plots the average[1] shock-speed (normalized with respect to its maximum value) versus the CFD iterations counter. The vertical bars shown in the same figure denote the maximum normalized displacement of the deformable structure obtained at each FSI iteration. During the first 1200 iterations the shield shape is kept fixed and the shock-speed is seen to decrease until steady-state is reached. Here we are at the end of Step 2, as described in § 2. In Step 3 the MSC Nastran structural solver is used to compute the new shape of the HIAD under the differential effect of the constant inflation pressure and aerodynamic pressure computed by the S-F solver in Step 1. Upon completion of Step 4, the shape of the impermeable surface of the shield has changed and a new CFD solution must be computed. This is accomplished during the next 600 CFD iterations, see Fig. 13: the average shock-speed is seen to rapidly increase at first, so as to modify the location and shape of the bow-shock, and then gradually decrease until a steady-state solution is again reached. After the third FSI

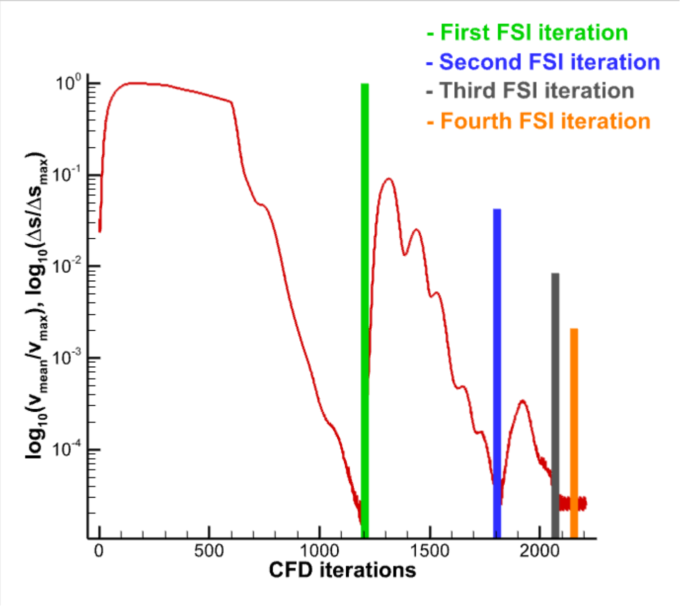

Figure 13: Mean shock velocity and maximum shield displacement plotted against the CFD iterations counter.

---

[1] the average is taken over all grid-points of the shock-surface triangulation

iteration, the displacement of the membrane has become so small that it no longer affects the flow-field. Therefore, already two or three FSI iterations suffice to obtain a reasonable iterative convergence. For all subsequent test-cases three FSI iterations will be used.

Figure 14(a) shows the pressure field in the YZ symmetry plane obtained at the end of the iterative procedure described by Fig. 13. Figure 14(b) allows to compare the final (marked in red) and initial (marked in black) shape of the inflatable shield. The effect of the prescribed constraints is noticeable for both the rigid nose, which moves upstream because the inflation pressure is larger than stagnation pressure, and the outer crown, which moves towards the Y-axis. Figure 14(c) allows to compare the initial and converged shock stand-off distance in the YZ symmetry plane.

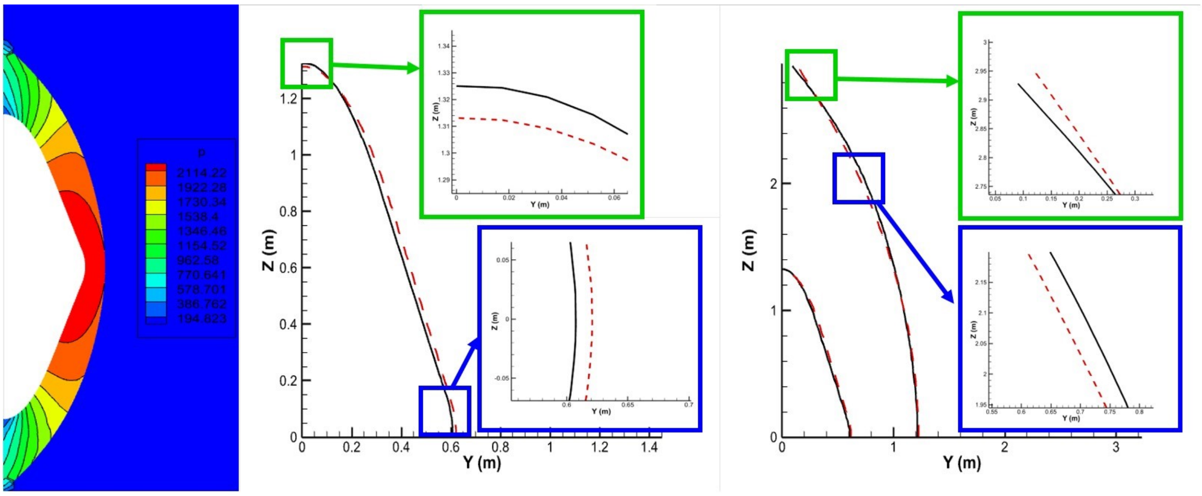

a) b) c)

Figure 14: a) Hypersonic flow past an inflatable shield: pressure field in the YZ symmetry plane; b) deformation of the inflatable shield in the YZ-plane; c) differences in the bow-shock stand-off distance between the initial and steady-state position. The black solid line marks the initial shape, the red dashed line the one at steady-state.

The advantages offered by fitting the bow-shock are evident when comparing Fig. 14(a) with the S-C calculation of Fig. 10(a), both computed on grids of nearly identical mesh spacing. In particular, the pressure field inside the shock layer[2] computed by S-F, see Fig. 14(a), is free from the severe disturbances that are seen in Fig. 10(a). This is a consequence of the unphysical thickness and meandering shape of the captured shock, which could only be remedied by using anisotropic mesh adaptation.

Figure 15 compares the wall pressure distribution computed on the two grid levels, which reveals good circumferential symmetry, even on the coarse grid and despite the use of a fully unstructured tetrahedralization. The capability of the S-F approach to supply high-quality solution even on coarse meshes implies substantial savings in computational cost.

One possibility to quantitatively asses the quality of a numerical solution when strong shocks are present consists in comparing the measured and design order-of-accuracy of the spatial discretization in regions of smooth-flow. S-C discretizations are known to degrade to first order-of-accuracy downstream of a captured shock, see [47], whereas S-F preserves design order also downstream of a fitted shock [19].

Total temperature is used to compute the measured order globally, because total temperature is constant throughout the whole flow-field. A local measure of the order-of-accuracy can be computed at stagnation point, because the bow shock is a normal shock on the stagnation streamline and the flow is brougth to rest isentropically behind the bow shock along the stagnation streamline; the stagnation pressure can therefore be analytically computed.

The results are reported in Table 5 and show that the measured order is indeed close to design order, $n = 2$, for both the global and local convergence analysis. This implies that both the coarse and the fine-grid solutions are in the asymptotic range of convergence, i.e. the terms in the discretization error of order higher than design order are negligible. Moreover, it is worth emphasizing that the total temperature error on the coarsest mesh is less that 0.1% of the freestream total temperature value and

---

[2] in the present context the shock-layer is the region bounded upstream by the bow-shock and downstream by the shield

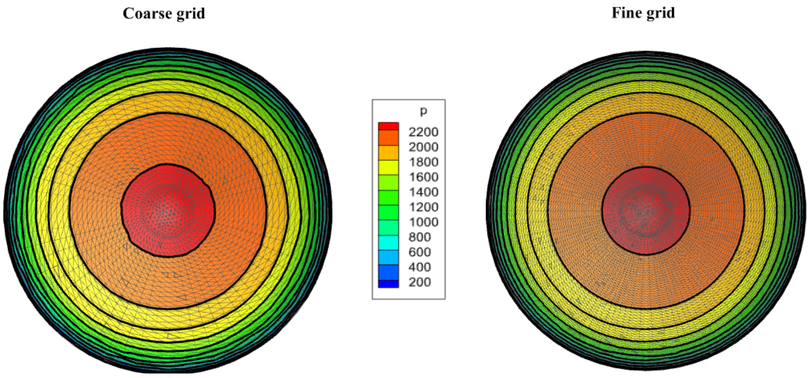

Figure 15: Wall pressure distribution on the coarse (left) and fine (right) grid levels

Grid level	$L_1(T^0_\infty - T^0_i)/T^0_\infty$	Computed p^h_{st}	$p_{\mathrm{st}} - p^h_{\mathrm{st}}$
1	5.718e-04	2304.53 Pa	2.92 Pa
2	1.608e-04	2306.60 Pa	0.85 Pa
$\tilde{n}$	1.83	1.78	

Table 5: Grid-convergence analyses: global based on total temperature; local based on stagnation pressure; the analytically computed stagnation pressure, p_{st} is given in Tab. 3.

the stagnation pressore discretization error is about 3 Pa which amounts to 0.1% of the exact stagnation pressure. These error estimates can be regarded as highly reliable because the numerical solutions are in asymptotic convergence.

3.2 Test-case 2: complete capsule configuration

In this second test-case we consider a more realistc geometry that includes a closed inflatable shield and a rigid afterbody.

The spacecraft shown in Figure 16 has the typical shape used for the orbital insertion of SmallSats using an aerocapture maneuver [48]. Figure 17, where the inflatable part of the structure is painted in green and the rigid one in blue, shows the shape of the shield when inflated to the design differential pressure of $p_{\mathrm{inf}} = 20$ kPa.

To model an initially loaded configuration in MSC Nastran, it is necessary to compute and then impose the initial stress state that balances the internal inflation pressure of the shield. Once the internal loads are balanced, the interaction with the external fluid dynamics field can be evaluated.

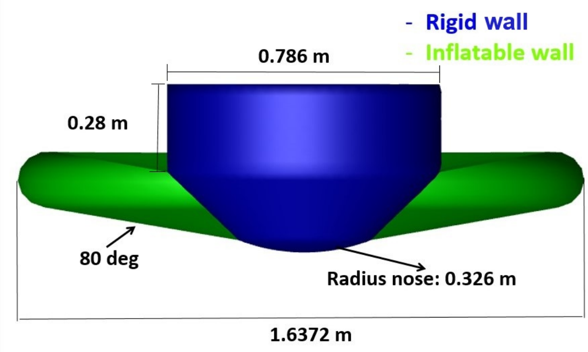

Figure 16: Geometry of the capsule

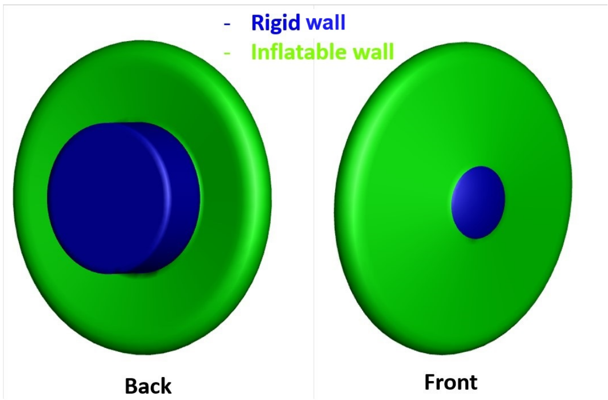

Figure 17: Front and back point of view

The flow conditions used for this test-case, see Tab. 6, are compatible with a single point of the trajectory during an aerocapture maneuver on Mars; the symbols have already been introduced by reference to Tab. 3.

M_∞	ρ_∞	p_∞	γ	R	p_{st}	T^0_∞
24	$2.60 \cdot 10^{-5}$ kg/m^3	0.73 Pa	1.33	191 J/kgK	526.40 Pa	12248.22 K

Table 6: Atmospheric conditions compatible with an aerocapture manouver on Mars.

Figure 18(a) shows the computational domain; the prescribed boundary conditions are given in Fig. 18(b).

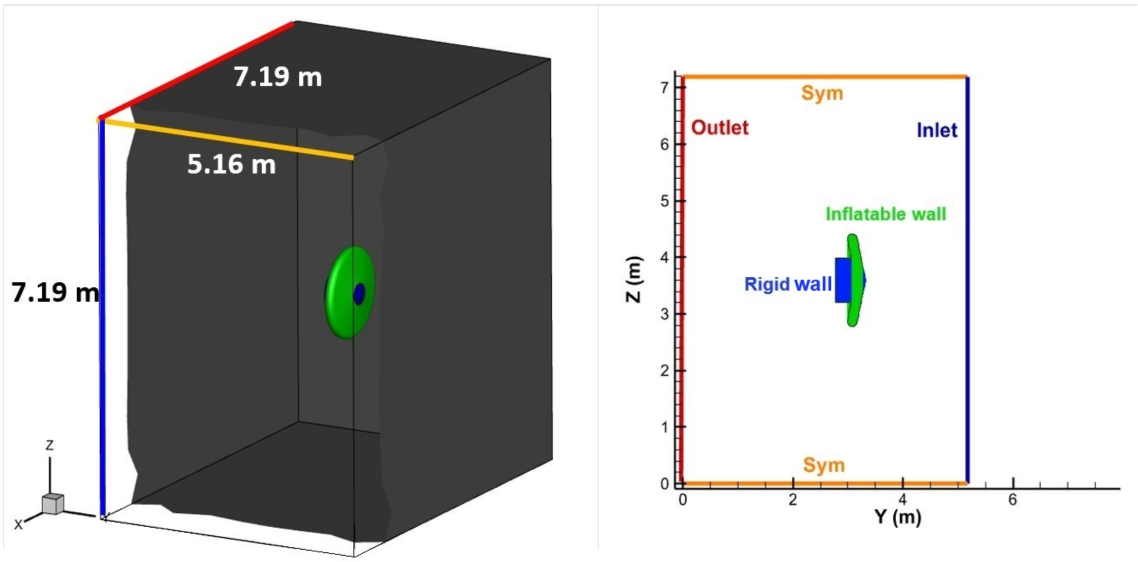

a) b)

Figure 18: a) Computational domain; b) prescribed boundary conditions.

The number of grid-points and cells of the background tetrahedral mesh and the two surface triangulations of the shock and the HIAD are reported in Tab. 7.

Background		Shield		Shock	
grid-points	tetrahedra	grid-points	triangles	grid-points	triangles
21957	128428	2961	5918	3832	7486

Table 7: Number of grid points and cells of the volumetric and surface meshes

The structural model uses the same material properties and simulation settings of the test-case examined in § 3.1, except for the initial stress field and the following nodal constraints:

- the grid-points that belong to the rigid nose and the afterbody have all degrees of freedom constrained, i.e. they are fixed in space;
- the grid-points of the inflatable part are free to translate in any direction, but the rotational degrees of freedom are blocked, as in the previous test-case.

Simulations have been run for three different values of the inflation pressure, two lower and one equal to the design inflation pressure, $p_{\mathrm{inf}} = 20$ kPa. The pressure field in the YZ symmetry plane obtained for the three different values of the inflation pressure is shown in Fig. 19 and the corresponding shapes of the bow shock and the HIAD in Fig.20. The comparison among the three frames of Fig. 20 clearly shows that by changing the inflation pressure, the shape and, to a lesser extent, the cross-sectional area of the shield are also affected. Both the cross-sectional area, A, and the shield-shape via the drag coefficient, C_D, affect the ballistic coefficient $\beta = m/C_D A$, m being the mass of the vehicle. The percentage variations of the ballistic coefficient, with respect to the case at 20 kPa, are reported in Tab. 8.

Table 9 gives the coordinates of three points in the YZ-plane picked up along the bow shock for the three different values of the inflation pressure. The point at $z = 0$ is the intersection between the

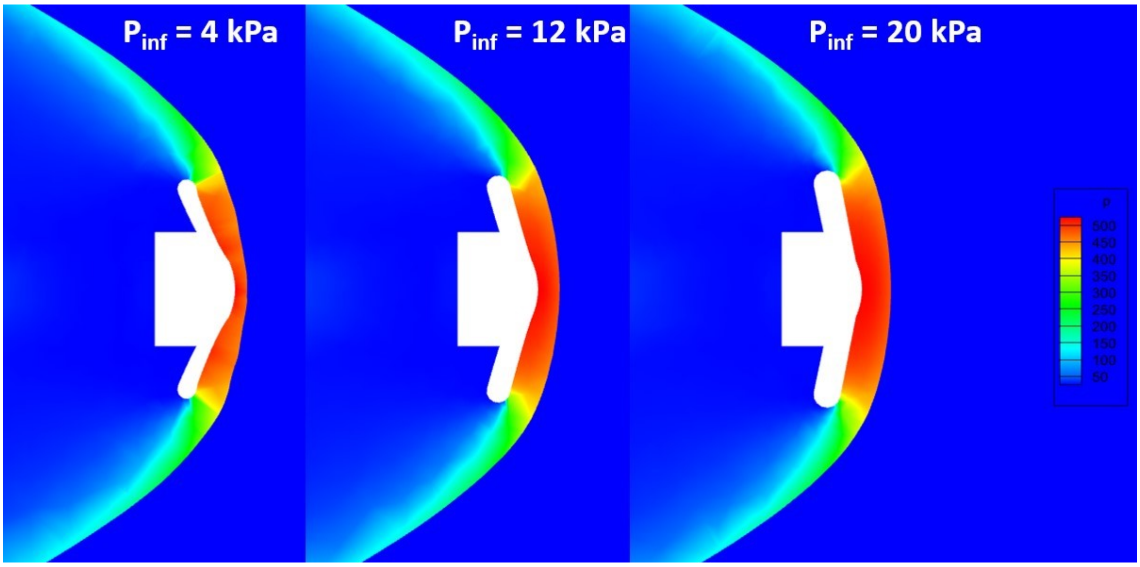

Figure 19: Pressure field in the YZ plane corresponding to three different inflation pressures, $p_{\mathbf{inf}} = 4$, 12, 20 kPa.

p_{inf}	Ballistic coefficient kg/m^2	percentage variation
20 kPa	15.66	-
12 kPa	17.74	+13.28%
4 kPa	21.21	+35.45%

Table 8: Percentage variations of the ballistic coefficient

stagnation streamline and the bow shock, see Fig. 19b), whereas the other two are farther away from the Y axis, see Fig. 19a). In all cases the displacement of the bow shock is remarkable.

z(m)	y at 4 kPa (m)	y at 12 kPa (m)	y at 20 kPa (m)
0	0.081	0.145	0.194
1	-0.355	-0.271	-0.188
2	-1.437	-1.351	-1.269

Table 9: Final shock positions for three different inflation pressures, $p_{\mathbf{inf}} = 4$, 12, 20 kPa.

3.3 Test-case 3: EFESTO configuration

This last test-case reproduces the EFESTO [49] shield, developed by the European Space Agency (ESA) for Mars reentry maneuvers. The EFESTO shield, which is displayed in Fig. 21 along with its geometrical features, is made of an inflated toroid connected to the rigid nose and rigid afterbody by two membranes. The two membranes are connected to the rigid structure and to the inflatable toroid using the three junctions that have been highlighted in Fig. 22. The presence of the junctions poses a minor challenge to our technique due to differences between the structural and CFD grids. This is because step 1 of the algorithm, see § 2, removes all grid-points of the background mesh that fall inside the inflatable structure where a spatially uniform pressure is prescribed. Therefore, as shown in Fig. 23, the toroidal structure is visible in the structural grid, but part of it is missing in the CFD mesh. This implies that there is not any longer a one-to-one correspondance between the grid-points of the surface meshes of the HIAD in the structural and CFD models. Apart from this, there are no major changes in the FSI coupling procedure compared to the previous test-cases. Freestream conditions are reported in Tab. 10 whereas the computational domain and prescribed boundary conditions are shown in Fig. 24(a) and Fig. 24(b), respectively.

Table 11 gives information about the volumetric and surface meshes used in the CFD model. The structural model uses the same material properties of the test-case examined in § 3.1, except for the

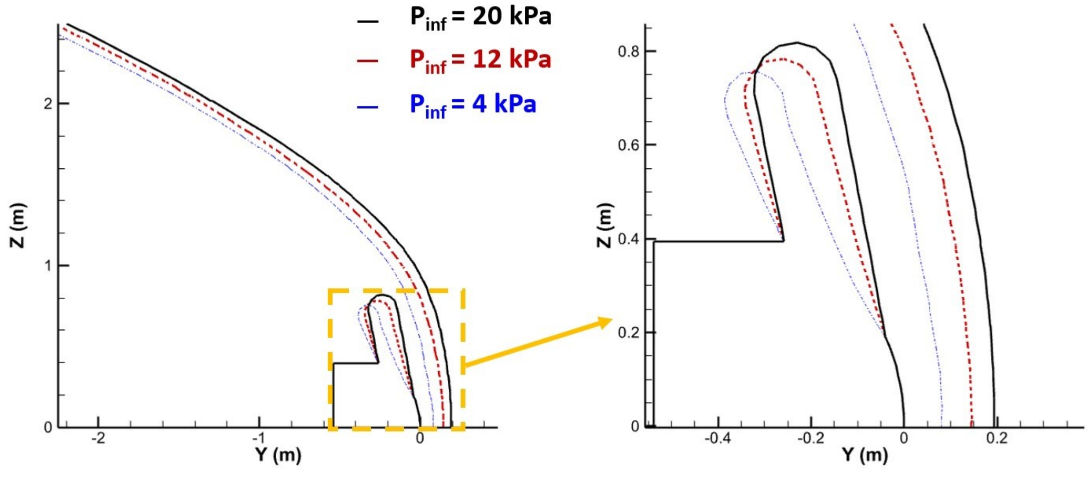

a) b)

Figure 20: Shock shape and structural deformation for three differents inflation pressures, $p_{\mathbf{inf}}$ = 4, 12, 20 kPa.

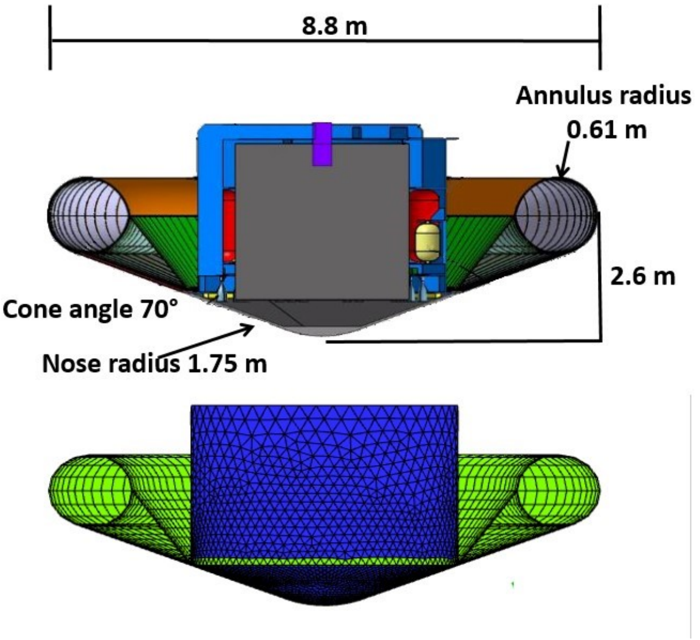

Figure 21: EFESTO heat shield configuration and structural mesh

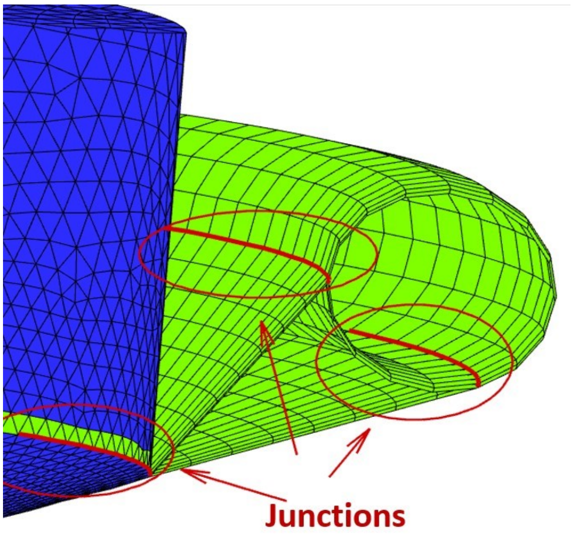

Figure 22: EFESTO structural junctions

M_∞	ρ_∞	p_∞	γ	R	p_{st}	T^0_∞
25	$1.98 \cdot 10^{-5}$ kg/m^3	0.65 Pa	1.33	191 J/kgK	254.39 Pa	18017.02 K

Table 10: Sample atmospheric conditions for Mars.

initial stress field and the fact that the translational degrees of freedom have been left unconstrained, while the rotational ones are kept fixed for the same reasons outlined in § 3.1. The only new feature to be modeled are the junctions: junction elements must have nodes where the translation is the same for all the different structural components that meet at the junction, see Fig. 22. This is made possible in MSC Nastran, which allows to impose identical translation in the connected mesh nodes of the junctions. Since we lack information regarding the material type and the inflation pressure of the toroid, we use the same material as in § 3.2 and the shape shown in Fig. 21 as the design shape corresponding to p_{inf}

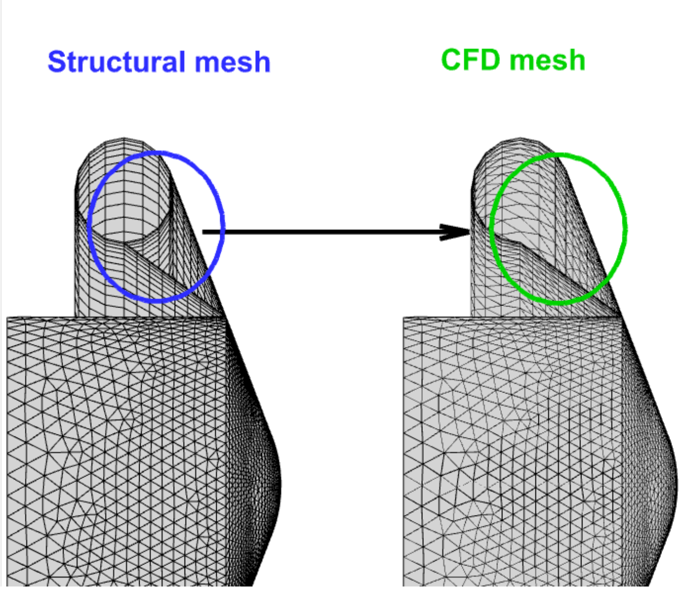

Figure 23: Differences between the structural and CFD models.

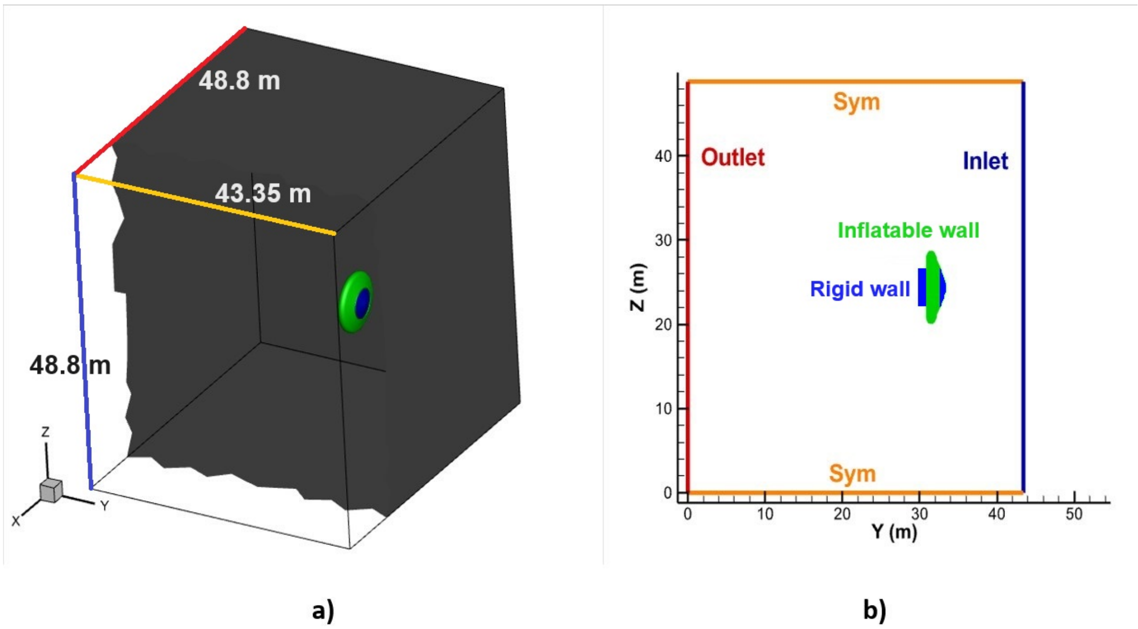

Figure 24: a) Orthogonal parallelepiped domain; b) Boundary conditions

Background-mesh		HIAD		Shock	
grid-points	tetrahedra	grid-points	triangles	grid-points	triangles
35671	209505	5621	11438	7530	14883

Table 11: Features of the background tetrahedral mesh and surface triangulations of the inflatable shield and bow shock

$= 20$ kPa inflation pressure.

The shape of the bow shock and that of the HIAD in the YZ-plane are shown in Fig. 25 for both the fully inflated and partly deflated configurations; the latter is obtained for an inflation pressure equal to $p_{\text{inf}} = 10$ kPa. Since the deformation of the HIAD is limited, the CFD solution corresponding to the fully inflated configuration is omitted, whereas the pressure field in the YZ symmetry plane obtained when deflating the HIAD at $p_{\text{inf}} = 10$ kPa is shown in Fig. 26. Table 12 shows the coordinates of three different points along the intersection between the bow shock the YZ-plane. The rightmost columns correspond to the two different values of the inflation pressure.

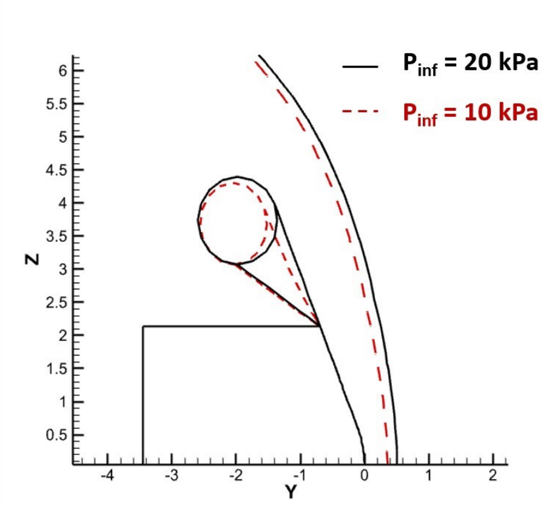

Figure 25: Structural deformation of the EFESTO heat-shield: fully inflated and partly deflated configurations.

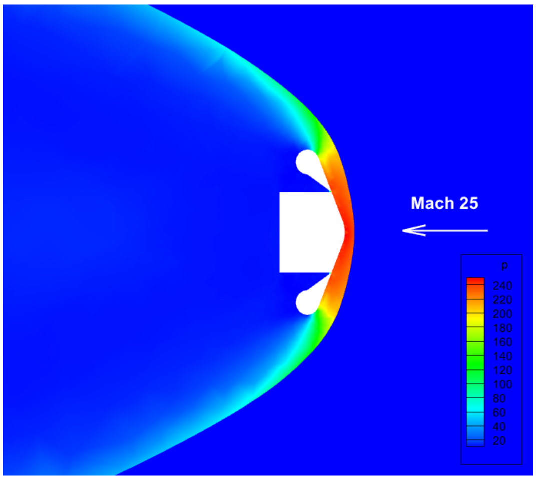

Figure 26: Pressure field around the EFESTO heat-shield in the YZ symmetry-plane when inflated at $p_{\text{inf}} = 10$ kPa

z(m)	y at 10 kPa (m)	y at 20 kPa (m)
0	0.355	0.505
3	-0.125	0.034
6	-1.46	-1.385

Table 12: Final shock positions for two different inflation pressures, $p_{\mathbf{inf}} = 10$, 20 kPa.

4 Conclusion and Future Work

A novel numerical technique for computing the Fluid-Structure interaction between a geometrically complex inflatable structure and an high-speed flow has been presented and discussed. The methodology originates from shock-fitting methods that explicitly identify and track the motion of gas-dynamic discontinuities using the Rankine-Hugoniot jump relations. Fitted shocks are modelled as internal boundaries of negligible thickness that bound regions of the flow-field where a smooth solution to the governing PDEs exists. A similar approach is used for the inflatable structure, which is modeled as a non-linear membrane using a commercial structural software. Using the three test-cases included in this paper, we show that the proposed approach takes advantage of one of the key features of shock-fitting, i.e. high quality solutions even on coarse meshes. In particular, local and global grid-convergence analyses reveal a measured order-of-convergence which is very close to design order and small discretization errors.

The only additional requirement for extending the technique to viscous flows is the capability to deform the boundary layer mesh to adapt to the deforming shape of the HIAD while retaining its topological integrity. Further developments include the modeling of non-isotropic material behaviour.

Acknowledgments

The scholarship supporting Dr. Valerio Orlandini is funded by the Ministry of University and Research in the framework of the “PNRR PhD scholarships ex Ministerial Decree 118/2023” titled “Development of an innovative aerocapture system for interplanetary missions”

References

[1] Stephen Hughes, Robert Dillman, Brett Starr, Ryan Stephan, Michael Lindell, Charles Player, and F. Cheatwood. Inflatable re-entry vehicle experiment (IRVE) design overview. In *18th AIAA Aerodynamic Decelerator Systems Technology Conference and Seminar*, 2005.

[2] Stephen Hughes, F. Cheatwood, Robert Dillman, Anthony Calomino, Henry Wright, Joseph DelCorso, and Anthony Calomino. Hypersonic inflatable aerodynamic decelerator (hiad)technology development overview. In *21st AIAA Aerodynamic Decelerator Systems Technology Conference and Seminar*, 2011.

[3] Daniel Litton, David Bose, F. Cheatwood, Stephen Hughes, Henry Wright, Michael Lindell, Stephen Derry, and Aaron Olds. *Inflatable Re-entry Vehicle Experiment (IRVE) - 4 Overview.* 2011.

[4] Hillary S. Blakeley, Richard J. Bodkin, and Anjie Emmett. *Heritage to Flight; The Test Program that Brought an Inflation System Back to Life.* 2024.

[5] John DiNonno and Neil Cheatwood. *Low-Earth Orbit Flight Test of an Inflatable Decelerator (LOFTID) Mission Overview and Science Return.* 2024.

[6] Detlef Wilde, Stephan Walther, Konstantin Pitchadze, Sergej Alexsaschkin, Dietrich Vennemann, and Lionel Marraffa. Flight test and iss application of the inflatable reentry and descent technology (irdt). *Acta Astronautica*, 51(1):83–88, 2002.

[7] Giuseppe Guidotti, Giuseppe Governale, Nicole Viola, Ingrid Dietleinc, Steffen Callsen, Kevin Bergmann, Junnai Zhai, Roberto Gardi, Barbara Tiseo, Ysolde Prevereaud, Yann Dauvois, Giovanni Gambacciani, and Giada Dammacco. Pushing the limits of re-entry technology: an overview of the Efesto-2 project and the advancements in inflatable heat shields. In *Aeronautics and Astronautics AIDAA XXVII International Congress*, volume 37, pages 576–580, 2023.

[8] Giuseppe Guidotti, Irene Pontijas Fuentes, Federico Trovarelli, Ingrid Dietlein, Thorn Schleutker, Roberto Gardi, Jean-Luc Verant, Ysolde Prevereaud, Yann Dauvois, and Giuseppe Governale. Efesto - advancing european hypersonic inflatable heatshield technology for earth recovery and mars high-mass delivery missions. *Aeronautics and Aerospace Open Access Journal*, 6:59–73, 2022.

[9] Valerio Orlandini, Renato Paciorri, Alessia Assonitis, Francesco Saltari, and Aldo Bonfiglioli. A fluid dynamics technique for modelling inflatable shield for re-entry or aerocapture missions. In *AIAA AVIATION 2023 Forum*, page 4425, 2023.

[10] Zachary R Putnam and Robert D Braun. Drag-modulation flight-control system options for planetary aerocapture. *Journal of Spacecraft and Rockets*, 51(1):139–150, 2014.

[11] Kenji Takizawa and Tayfun E. Tezduyar. Computational methods for parachute fluid–structure interactions. *Archives of Computational Methods in Engineering*, 19(1):125–169, Mar 2012.

[12] Joung-Dong Kim, Yan Li, and Xiaolin Li. Simulation of parachute FSI using the front tracking method. *Journal of Fluids and Structures*, 37:100–119, 2013.

[13] Jonathan Boustani, Michael F Barad, Cetin C Kiris, and Christoph Brehm. Fully-coupled fluid-structure interaction simulations of a supersonic parachute. In *AIAA Aviation 2019 Forum*, page 3279, 2019.

[14] Sheng Gong and Chuijie Wu. A study of a supersonic capsule/rigid disk-gap-band parachute system using large-eddy simulation. *Applied Mathematics and Mechanics*, 42(4):485–500, Apr 2021.

[15] Tayfun E. Tezduyar. Finite element methods for flow problems with moving boundaries and interfaces. *Archives of Computational Methods in Engineering*, 8(2):83–130, Jun 2001.

[16] M.D. Salas. *A Shock-Fitting Primer.* CRC Applied Mathematics & Nonlinear Science. Chapman & Hall, 1^{st} edition, 2009.

[17] D.L. Bonhaus. *A higher order accurate finite element method for viscous compressible flows.* PhD thesis, Virginia Polytechnic Institute and State University, 1998.

[18] Mark H. Carpenter and Jay H. Casper. Accuracy of Shock Capturing in Two Spatial Dimensions. *AIAA Journal*, 37(9):1072–1079, September 1999.

[19] Aldo Bonfiglioli and Renato Paciorri. Convergence analysis of shock-capturing and shock-fitting solutions on unstructured grids. *AIAA journal*, 52(7):1404–1416, 2014.

[20] Aldo Bonfiglioli, Marco Grottadaurea, Renato Paciorri, and Filippo Sabetta. An unstructured, three-dimensional, shock-fitting solver for hypersonic flows. *Computers & Fluids*, 73:162–174, 2013.

[21] Alessia Assonitis, Renato Paciorri, Carl F Ollivier Gooch, and Aldo Bonfiglioli. 3D flow computations over blunt bodies at hypersonic speeds using shock-fitting technique. In *AIAA AVIATION 2022 Forum*, page 3989, 2022.

[22] Michael Lindell, Stephen Hughes, Megan Dixon, and Cliff Willey. Structural analysis and testing of the inflatable re-entry vehicle experiment (IRVE). In *47th AIAA/ASME/ASCE/AHS/ASC*

Structures, Structural Dynamics, and Materials Conference, 2006.

[23] Jie Wu, Zhang Zhang, Anping Hou, Meifang Zhu, and Qi Wang. Nonlinear structural dynamics of the inflatable re-entry vehicle experiment (IRVE). In *22nd AIAA International Space Planes and Hypersonics Systems and Technologies Conference*, page 5204, 2018.

[24] Hang Si. Tetgen, a delaunay-based quality tetrahedral mesh generator. *ACM Trans. Math. Softw.*, 41(2), feb 2015.

[25] G. Balarac, F. Basile, P. Bénard, F. Bordeu, J.-B. Chapelier, L. Cirrottola, G. Caumon, C. Dapogny, P. Frey, A. Froehly, G. Ghigliotti, R. Laraufie, G. Lartigue, C. Legentil, R. Mercier, V. Moureau, C. Nardoni, S. Pertant, and M. Zakari. Tetrahedral remeshing in the context of large-scale numerical simulation and high performance computing. *MathematicS In Action*, 11(1):129–164, 2022.

[26] Aldo Bonfiglioli. Fluctuation splitting schemes for the compressible and incompressible euler and navier-stokes equations. *International Journal of Computational Fluid Dynamics*, 14(1):21–39, 2000.

[27] Aldo Bonfiglioli and Renato Paciorri. A mass-matrix formulation of unsteady fluctuation splitting schemes consistent with Roe's parameter vector. *International Journal of Computational Fluid Dynamics*, 27(4-5):210–227, 2013.

[28] Carl F. Ollivier Gooch. The GRUMMP mesh generator.

[29] M. Ricchiuto and R. Abgrall. Explicit Runge-Kutta residual distribution schemes for time dependent problems: Second order case. *Journal of Computational Physics*, 229(16):5653 – 5691, 2010.

[30] L. Arpaia, M. Ricchiuto, and R. Abgrall. An ALE formulation for explicit Runge-Kutta residual distribution. *Journal of Scientific Computing*, pages 1–46, 2014.

[31] Mario Ricchiuto. An explicit residual based approach for shallow water flows. *Journal of Computational Physics*, 280:306 – 344, 2015.

[32] Lorenzo Campoli, Alessia Assonitis, Mirco Ciallella, Renato Paciorri, Aldo Bonfiglioli, and Mario Ricchiuto. UnDiFi-2D: an unstructured discontinuity fitting code for 2d grids. *Computer Physics Communications*, 271:108202, 2022.

[33] *MSC Nastran 2023.3 Nonlinear (SOL 400) User's Guide*, 2023.

[34] James Serrin. Mathematical principles of classical fluid mechanics. In *Fluid Dynamics I/Strömungsmechanik I*, pages 125–263. Springer, 1959.

[35] Alphose Zingoni. Membrane solutions for shells of revolution under non-axisymmetric loading. In *Shell Structures in Civil and Mechanical Engineering: Theory and analysis*, pages 123–134. ICE Publishing, 2017.

[36] Herman Deconinck and Mario Ricchiuto. *Residual Distribution Schemes: Foundations and Analysis*, pages 1–53. John Wiley & Sons, Ltd, 2017.

[37] R. Abgrall and Mario Ricchiuto. *High-Order Methods for CFD*, pages 1–54. John Wiley & Sons, Ltd, 2017.

[38] Patrick Roache. Error Bars for CFD. In *41st Aerospace Sciences Meeting and Exhibit.* American Institute of Aeronautics and Astronautics (AIAA), jan 2003. 41st Aerospace Sciences Meeting and Exhibit, Reno, Nevada, Jan. 6-9, Paper 2003-408.

[39] L. Eça and M. Hoekstra. A verification exercise for two 2-d steady incompressible turbulent flows. In P. Neittaanaki, T. Rossi, K. Majava, and O. Pironneau, editors, *Proceedings of the ECCOMAS*, 2004. Jyaskya, 24–28 July 2004.

[40] J. Franke and W. Frank. Application of generalized richardson extrapolation to the computation of the flow across an asymmetric street intersection. *Journal of Wind Engineering and Industrial Aerodynamics*, 96(10-11):1616 – 1628, 2008. 4th International Symposium on Computational Wind Engineering (CWE2006).

[41] Xavier De Saint Victor. Estimation of the accuracy of numerical simulations using richardson extrapolation and a hessian technique. *International Journal of Engineering Systems Modelling and Simulation*, 2(1-2):25–37, 2010.

[42] *MSC Nastran 2023.4 Linear Static Analysis User's Guide*, 2023.

[43] Matthew P Golombek. The Mars Pathfinder mission. *Journal of geophysical research: Planets*, 102(E2):3953–3965, 1997.

[44] MatWeb LLC. Matweb: Online materials information resource.

[45] Kurt Snmalley, Michael Tinker, and Richard Fischer. Investigation of nonlinear pressurization and modal restart in MSC/NASTRAN for modeling thin film inflatable structures. In *19th AIAA Applied Aerodynamics Conference*, page 1409, 2001.

[46] Kurt B Smalley, Michael L Tinker, and W Scott Taylor. Structural modeling of a five-meter thin-film inflatable antenna/concentrator. *Journal of spacecraft and rockets*, 40(1):27–29, 2003.

[47] J. Casper and M. Carpenter. Computational considerations for the simulation of shock-induced

sound. *SIAM Journal on Scientific Computing*, 19(3):813–828, 1998.

[48] Rohan Deshmukh, Angela Bowes, and Soumyo Dutta. Small satellite aerocapture concepts for future interplanetary missions. In *AIAA SCITECH 2023 Forum*, page 0877, 2023.

[49] Federico Trovarelli, Giuseppe Guidotti, Giovanni Medici, Thorn Schleutker, Burkard Esser, Ingrid Monika Dietlein, Giovanni Gambacciani, Giuseppe Governale, Jean-Luc Verant, Yann Dauvois, et al. Advanced european re-entry system based on inflatable heat shields efesto project overview: system and mission design and technology roadmap. In *72ND INTERNATIONAL ASTRONAUTICAL CONGRESS (IAC 2021)*, pages IAC–21, 2021.